

## An almanac of predicted microlensing events for the 21st century

D.M. Bramich<sup>1</sup> and M.B. Nielsen<sup>2</sup>

<sup>1</sup>New York University Abu Dhabi, PO Box 129188, Saadiyat Island, Abu Dhabi, UAE  
e-mail: dan.bramich@hotmail.co.uk

<sup>2</sup>Center for Space Science, NYUAD Institute, New York University Abu Dhabi, PO Box  
129188, Abu Dhabi, UAE  
e-mail: mbn4@nyu.edu

*Received July 6th, 2018*

### ABSTRACT

Using *Gaia* data release 2 (GDR2), we present an almanac of 2,509 predicted microlensing events, caused by 2,130 unique lens stars, that will peak between 25th July 2026 and the end of the century. This work extends and completes a thorough search for future microlensing events initiated by Bramich (2018) and Nielsen & Bramich (2018) using GDR2. The almanac includes 161 lenses that will cause at least two microlensing events each. A few highlights are presented and discussed, including: (i) an astrometric microlensing event with a peak amplitude of  $\sim 9.7$  mas, (ii) an event that will probe the planetary system of a lens with three known planets, and (iii) an event (resolvable from space) where the blend of the lens and the minor source image will brighten by a detectable amount ( $\sim 2$  mmag) due to the appearance of the minor source image. All of the predicted microlensing events in the almanac will exhibit astrometric signals that are detectable by observing facilities with an angular resolution and astrometric precision similar to, or better than, that of the *Hubble Space Telescope* (e.g. NIRCam on the *James Webb Space Telescope*), although the events with the most extreme source-to-lens contrast ratios may be challenging. Ground-based telescopes of at least 1 m in diameter can be used to observe many of the events that are also expected to exhibit a photometric signal.

**Key words:** *gravitational lensing: micro – methods: data analysis – catalogs – astrometry – stars: fundamental parameters*

### 1. Introduction

With the recent second data release from the *Gaia* satellite (GDR2; Prusti et al. 2016; Brown et al. 2018), there has been a flurry of new work and interest on the subject of predicting microlensing events (Klüter et al. 2018; Bramich 2018; Mustill, Davies & Lindegren 2018; Ofek 2018; Nielsen & Bramich 2018). An analysis of the Tycho *Gaia* Astrometric Solution (TGAS) for  $\sim 2$  million stars from the first *Gaia* data release (Lindegren et al. 2016) only yielded a single microlensing event prediction; namely, for the white dwarf star LAWD 37 (McGill et al.

2018). However, GDR2 far surpasses TGAS, and any other astrometric catalogue in existence today, in terms of its all-sky coverage, number of objects, sample volume (depth), and astrometric precision and accuracy. With  $\sim 1.7$  billion objects, of which  $\sim 1.3$  billion have 5-parameter astrometric solutions, GDR2 can act as a catalogue of both microlensing source and lens stars (e.g. Bramich 2018; hereafter B18), or simply as an all-sky catalogue of source stars down to  $\sim 21$  mag (e.g. Nielsen & Bramich 2018). Pre-*Gaia* work on this topic has lacked sufficiently precise astrometric input catalogues resulting in rather uncertain and unreliable predictions (e.g. Feibelman 1966; Salim & Gould 2000; Proft, Demleitner & Wambsganss 2011). Consequently, only one predicted event has been successfully detected up until now. Sahu et al. (2017) predicted a microlensing event for Stein 2051 B (also independently predicted by Proft, Demleitner & Wambsganss 2011) and they acquired appropriate *Hubble Space Telescope (HST)* observations which allowed them to measure the mass of this white dwarf as  $\sim 0.675 M_{\odot}$  with an uncertainty of  $\sim 8\%$ .

Microlensing events can be used to directly measure the masses of single isolated stars (e.g. Yoo et al. 2004; Yee et al. 2009; Zhu et al. 2016), for which so few measurements exist ( $\lesssim 15$ ), and to find planetary mass companions to the lenses (e.g. Beaulieu et al. 2006). Specifically, for bright lenses (i.e. lenses whose flux is detected), the astrometric lensing signal alone enables the lens mass to be determined to within  $\sim 1\text{-}10\%$  (Sahu et al. 2017). Since directly measured stellar masses, estimated independently of the assumed internal physics, come mostly from observations of the orbital motion of binary stars (Torres, Andersen & Giménez 2010), astrometric microlensing provides an important channel to direct mass measurements of single stars. Microlensing events that exhibit both photometric and astrometric signals provide even stronger constraints on the physical properties of the lens by allowing important parameter degeneracies to be broken (Høg, Novikov & Polnarev 1995; Miyamoto & Yoshii 1995; Walker 1995). High-magnification photometric events (e.g. Udalski et al. 2005) provide an excellent opportunity for exoplanet detection. The key to these microlensing applications is to obtain good data coverage of an event from beginning-to-end to allow full characterisation. Predicting microlensing events in advance is therefore advantageous for planning and executing the necessary observations.

The analysis of GDR2 as both a source and a lens catalogue for microlensing predictions is currently incomplete. The current status is as follows. Klüter et al. (2018) present three cherry-picked event predictions for the stars Luyten 143-23 (two events in 2018 and 2021) and Ross 322 (one event in 2018)<sup>1</sup>. B18, who performed a thorough search of GDR2 over the (extended) lifetime of the *Gaia* satellite, report on 76 predicted events peaking between July 2014 and July 2026. B18 independently find the predicted Ross 322 event from Klüter et al. (2018; event

---

<sup>1</sup>We note that only the predictions for Luyten 143-23 are new. The predicted event for Ross 322 corresponds to predicted event #37 from Proft, Demleitner & Wambsganss (2011).

ME25 in B18), and refine the predicted LAWD 37 event from McGill et al. (2018; event ME4 in B18), thereby verifying the reliability of the predictions of all three groups. Furthermore, B18 present eight more microlensing event predictions for LAWD 37 over the next decade. However, the predicted events for Luyten 143-23 from Klüter et al. (2018) are not in the list of events from B18 because this star fails the B18 lens star selection criteria on two counts. Luyten 143-23 is flagged in GDR2 as a “duplicated source” that is likely to have astrometric and/or photometric problems, and also its astrometric solution suffers from highly significant excess noise ( $\text{ASTROMETRIC\_EXCESS\_NOISE\_SIG} = 18.0$ ; dimensionless quantity in multiples of sigma).

Mustill, Davies & Lindegren (2018) focussed on finding photometric microlensing events that will occur in the next two decades (up until July 2035). They provide a list of 30 predicted photometric events, although only six of them are expected to reach a peak magnification above  $\sim 0.4$  mag (the bright-limit photometric precision of *Gaia*). Surprisingly, none of the 30 predicted events appear in the list of events from B18 (or in the almanac presented in this paper). A detailed inspection of the GDR2 data for the 30 lens stars reveals that all of them exhibit highly significant excess noise in their astrometric solutions ( $3.3 < \text{ASTROMETRIC\_EXCESS\_NOISE\_SIG} < 78.4$ ) and consequently they were rejected from the B18 lens star sample (who adopt the requirement  $\text{ASTROMETRIC\_EXCESS\_NOISE\_SIG} < 3$ ). Furthermore, two of the lens stars have parallax errors greater than 0.4 mas, indicating spurious astrometric solutions (see Section 4.2.6 in B18), and another lens star is a duplicated source. Further evidence of poor astrometric solutions for these lens stars comes from the reduced chi-squared values of the fits, which are  $>2$  for most of them and  $\sim 17.1$  in the worst case. Considering also that the Mustill, Davies & Lindegren (2018) analysis should have independently found at least some of the photometric events presented in B18 and in this paper (e.g. event ME19 which will produce a photometric signal with a  $\pm 1$ -sigma range between  $\sim 0.039$ -0.158 mag in late 2019), and that they did not correct for the underestimated uncertainties on the parameters of the astrometric solutions (Brown et al. 2018), we can only conclude that their predictions should be treated with caution and confirmed by independent calculations.

While working on the B18 paper, we realised that the astrometry in GDR2 is actually precise enough to enable reliable microlensing predictions well past the end of any extended *Gaia* mission and, in some of the more favourable cases, up to the end of the 21st century. Hence, we have extended the analysis from B18 to complete a thorough search of GDR2 for source-lens pairs that will produce microlensing events in the last  $\sim 75$  years of this century. The almanac of events presented in this paper corresponds specifically to bright lenses present in GDR2. For faint lenses that do not appear in GDR2, there is still plenty of opportunity for predicting microlensing events (e.g. Nielsen & Bramich 2018; Ofek 2018).

The purpose and scope of this paper is to provide an almanac of predicted mi-

cro lensing events for the 21st century that can be observed with existing or planned observing facilities. For instance, all of the predicted events in the almanac have been selected such that they will exhibit large enough astrometric signals to be detectable by observing facilities with an angular resolution and astrometric precision similar to, or better than, that of the *HST* (White 2006; Hoffmann & Anderson 2017), although the events with the most extreme source-to-lens contrast ratios may be challenging. Some of the events are also expected to exhibit a photometric signal, and in these special cases, ground-based telescopes (typically at least 1 m in diameter) can be used for the photometric observations. The *James Webb Space Telescope*<sup>2</sup>, due to be launched in early 2021, is suitably equipped with NIRC*am* (point-spread function full-width at half-maximum of 0.064''; wavelength coverage 0.6-5  $\mu\text{m}$ ) for the follow-up of the first events in the almanac, which will already be rising to their peaks in the years before July 2026. The source-to-lens contrast ratio for many events (especially those with white dwarf lenses) is greatly improved in the NIR wavebands, and coronagraphs are available for the most difficult cases. Technology advances at such a pace that observations of the predicted events in the latter half of the almanac will likely be routine.

The rest of this paper is organised as follows. In Section 2, we provide a brief description of the methods used to identify the predicted events. The details and format of the almanac are presented in Section 3. Finally, in Section 4, we highlight some interesting predicted events in the sample.

## 2. Methods

### 2.1. Source-Lens Pair Selection

The methods used for identifying source-lens pairs from GDR2 that could potentially lead to microlensing events follow those described in B18 with some very minor modifications. Hence the reader is referred to B18 if further details are required. Throughout this section and the rest of the paper, GDR2 data column names are written in TYPEWRITER font.

We correct the GDR2 parallaxes by adding 0.029 mas to the PARALLAX entries (Lindegren et al. 2018) and we inflate the uncertainties on the astrometric parameters by 25% (Brown et al. 2018). We then select lens stars from GDR2 using the constraints listed in Table 1. These constraints are the same as in B18, except that an extra requirement that a lens star should have  $G_{\text{BP}}$  and  $G_{\text{RP}}$  photometry has been imposed. This avoids having to employ any external catalogues for lens mass estimation later on. Note that the constraint  $\sigma[\varpi] < 0.4$  mas, which was applied at a later stage in the data processing in B18, has been moved to the initial lens selection in Table 1. Application of these constraints to GDR2 yields  $N_{\text{L}}=128,270,876$  potential lens stars. For the source stars, we use exactly the same sample that was

---

<sup>2</sup><https://jwst.nasa.gov/index.html>

Table 1: List of constraints that need to be satisfied in order for a GDR2 object to be selected as a lens star. The symbols  $\varpi$  and  $\sigma[\varpi]$  represent the corrected parallax and its inflated uncertainty, respectively. Furthermore,  $\chi^2 = \text{ASTROMETRIC\_CHI2\_AL}$ ,  $\nu = \text{ASTROMETRIC\_N\_GOOD\_OBS\_AL} - 5$ ,  $L(G) = 1.2 \max\{1, \exp[0.2(19.5 - G)]\}$ , and  $G = \text{PHOT\_G\_MEAN\_MAG}$ .

GDR2 Column Name	Relation	Value	Unit	Description
DUPLICATED_SOURCE	=	FALSE	-	Reject duplicated objects that are likely to have astrometric and photometric problems
FRAME_ROTATOR_OBJECT_TYPE	=	0	-	Reject known extra-galactic objects
ASTROMETRIC_PARAMS_SOLVED	=	31	-	Only accept objects that have a 5-parameter astrometric solution
$\varpi/\sigma[\varpi]$	>	4	-	Only accept objects with a sufficiently precise parallax measurement
$\varpi$	>	0	mas	Reject objects with a non-positive parallax
$\varpi$	<	769	mas	Reject objects with a parallax greater than that of Proxima Centauri, which has a <i>Gaia</i> parallax of $768.529 \pm 0.254$ mas
$\sigma[\varpi]$	<	0.4	mas	Reject objects with a spurious astrometric solution
$\sqrt{\chi^2/\nu}$	<	$L(G)$	-	Reject objects with a spurious astrometric solution
ASTROMETRIC_EXCESS_NOISE_SIG	<	3	-	Reject objects with significant excess noise in the astrometric solution
PHOT_BP_MEAN_MAG	$\neq$	NaN	mag	Reject objects that do not have $G_{BP}$ -band photometry
PHOT_RP_MEAN_MAG	$\neq$	NaN	mag	Reject objects that do not have $G_{RP}$ -band photometry

selected in B18, which consists of  $N_S=1,366,072,323$  stars.

The angular scale-size inherent to a microlensing event is defined by the Einstein radius:

$$\theta_E = \sqrt{\frac{4GM_L}{c^2} (\varpi_L - \varpi_S)} \quad (1)$$

where  $G$  is the gravitational constant,  $c$  is the speed of light,  $M_L$  is the lens mass, and  $\varpi_L$  and  $\varpi_S$  are the lens and source parallaxes, respectively. We perform the initial source-lens pair selection by computing a conservative upper limit  $\theta_{E,\max}$  on the value of the Einstein radius  $\theta_E$  for any particular source-lens pair by assuming a maximum lens mass of  $M_{L,\max} = 10M_\odot$ , a maximum lens parallax of  $\varpi_{L,\max} = \varpi_L + 3\sigma[\varpi_L]$  (where  $\sigma[\varpi_L]$  is the uncertainty on the lens parallax  $\varpi_L$ ), and a source parallax of zero. This is translated into a maximum source-lens angular separation  $\theta_{\text{det}}$  within which a microlensing signal can be detected by considering the astrometric deflections (which have a larger range of influence than the photometric magnifications) and the best astrometric precision achievable by any current observing facility in a single observation (excluding radio interferometry). One obtains  $\theta_{\text{det}} = \theta_{E,\max}^2/0.030$  mas, where 0.030 mas is the bright-limit along-scan astrometric precision for *Gaia* (Rybicki et al. 2018; B18).

For each potential lens star, we calculate the value of  $\theta_{\text{det}}$ . The minimum, median, and maximum values of  $\theta_{\text{det}}$  over all lens stars are  $\sim 0.27$ , 2.69, and 826 arc-

sec, respectively. To account (very) conservatively for source and lens motions, and for errors in the astrometric parameters, we compute the following quantity for each source-lens pair:

$$\begin{aligned}
\theta'_{\text{det}} = & \theta_{\text{det}} + 3\sigma[\alpha_{*,\text{ref},\text{S}}] + 3\sigma[\alpha_{*,\text{ref},\text{L}}] + 3\sigma[\delta_{\text{ref},\text{S}}] + 3\sigma[\delta_{\text{ref},\text{L}}] \\
& + T_{\text{rem}} (|\mu_{\alpha^*,\text{S}}| + 3\sigma[\mu_{\alpha^*,\text{S}}] + |\mu_{\alpha^*,\text{L}}| + 3\sigma[\mu_{\alpha^*,\text{L}}]) \\
& + T_{\text{rem}} (|\mu_{\delta,\text{S}}| + 3\sigma[\mu_{\delta,\text{S}}] + |\mu_{\delta,\text{L}}| + 3\sigma[\mu_{\delta,\text{L}}]) \\
& + \varpi_{\text{S}} + 3\sigma[\varpi_{\text{S}}] + \varpi_{\text{L}} + 3\sigma[\varpi_{\text{L}}]
\end{aligned} \tag{2}$$

where  $\sigma[\alpha_{*,\text{ref}}]/\cos(\delta_{\text{ref}})$ ,  $\sigma[\delta_{\text{ref}}]$ ,  $\sigma[\mu_{\alpha^*}]$ ,  $\sigma[\mu_{\delta}]$ , and  $\sigma[\varpi]$  are the uncertainties on  $\alpha_{\text{ref}}$  (RA),  $\delta_{\text{ref}}$  (DEC),  $\mu_{\alpha^*}$  (PMRA),  $\mu_{\delta}$  (PMDEC), and  $\varpi$  (PARALLAX), respectively, and  $T_{\text{rem}} = 84.5$  years is the length of time from the GDR2 reference epoch (J2015.5) until the end of the 21st century (J2100.0). The subscripts S and L correspond to the source and the lens, respectively. We reject all source-lens pairs for which the angular distance between them at time  $t = \text{J2015.5}$  exceeds  $\theta'_{\text{det}}$ . This leaves 80,611,203 source-lens pairs, with 38,608,663 unique lenses, for further consideration.

We refine the source-lens pair selection as follows. For each lens star, we compute an approximate lens mass using the lens parallax, its mean  $G$ -band magnitude, the relation  $L/L_{\odot} \approx (M/M_{\odot})^4$  for main sequence stars more massive than the Sun, and by adopting  $M_{\text{bol},\odot} \approx 4.74$  mag. To conservatively account for extinction and bolometric corrections,  $M_{\text{L,max}}$  is set to four times the lens mass estimate. For giant stars,  $M_{\text{L,max}}$  is over-estimated since they are more luminous than main sequence stars, and hence the value of  $M_{\text{L,max}}$  computed in this way also serves as a maximum lens mass for giant stars. If  $M_{\text{L,max}}$  is less than the Chandrasekhar limit, then we increase it to  $1.44M_{\odot}$  to cover the possibility that the lens is a white dwarf, which also serves as an upper limit to the lens mass for sub-solar mass main sequence stars and brown dwarfs. We then recompute  $\theta_{\text{E,max}}$  for each source-lens pair using these improved upper limits on the lens masses.

We convert the new value of  $\theta_{\text{E,max}}$  for each source-lens pair into an improved maximum detection radius  $\theta_{\text{det}}$  by considering the asymptotic behaviour of the photometric and astrometric lensing signals in both the unresolved and partially-resolved microlensing regimes (see Section 4.2.5 in B18 for details), and by adopting the bright-limit photometric and astrometric precision of *Gaia* for a single observation (averaged over all possible scanning angles). These limits are 0.4 mmag for photometric observations (widely applicable to ground-based telescopes and of the correct order of magnitude for space telescopes - e.g. *HST*) and 0.131 mas for astrometric observations (similar to the best astrometric precision achievable by *HST* of  $\sim 0.2$  mas, e.g. Kains et al. 2017). The minimum, median, and maximum values of the improved  $\theta_{\text{det}}$  over all source-lens pairs are  $\sim 0.12$ , 0.22, and 29.6 arcsec, respectively.

For each source-lens pair, we consider their paths on the sky during the time period 25th July 2026 ( $t = 2461246.5$  BJD[TDB]) and 1st January 2100 ( $t = 2488069.5$  BJD[TDB]). The start of this time period coincides with the end of the time period considered in B18. To compute the parallax factors for an object at any time  $t$ , we use tabulated values of the Solar-system barycentric coordinates of the Earth (J2000.0 reference epoch;  $X(t)$ ,  $Y(t)$  and  $Z(t)$  in au; see Section 7.2.2.3 in Urban & Seidemann 2013) provided at daily intervals for the 21st century by the Jet Propulsion Laboratory HORIZONS on-line ephemeris computation service<sup>3</sup>. We employ cubic spline interpolation to calculate  $X(t)$ ,  $Y(t)$  and  $Z(t)$  from these data for any time  $t$ . We reject all source-lens pairs that do not approach each other to within an angular distance of less than  $\theta_{\text{det}}$  during the adopted time period. After performing this filtering step for each source-lens pair, we have 57,744 source-lens pairs remaining, with 53,741 unique lenses.

To filter out binary and co-moving source-lens pairs, and source-lens pairs where the lens is more distant than the source, we reject all source-lens pairs with  $\Delta\varpi/\sigma[\Delta\varpi] < 3$  where:

$$\frac{\Delta\varpi}{\sigma[\Delta\varpi]} = \frac{\varpi_L - \varpi_S}{(\sigma[\varpi_L]^2 + \sigma[\varpi_S]^2)^{1/2}} \quad (3)$$

We also reject all source-lens pairs for which the signal-to-noise ratio of the total relative proper motion is less than 3. At this point we now have 43,423 source-lens pairs remaining, with 39,545 unique lenses.

Finally, with  $\Delta\varpi$  guaranteed to be positive, we recompute the improved maximum detection radius  $\theta_{\text{det}}$  for the latest set of source-lens pairs using the improved upper limit on the lens mass  $M_{L,\text{max}}$  and adopting  $\Delta\varpi_{\text{max}} = \Delta\varpi + 3\sigma[\Delta\varpi]$ , which takes into account the source parallax (when available). By rejecting all source-lens pairs that do not approach each other to within an angular distance of less than  $\theta_{\text{det}}$  during the adopted time period, we are left with a final sample that consists of 42,572 source-lens pairs, with 38,717 unique lenses.

## 2.2. Lens Mass Estimation

To be able to predict microlensing events and their properties from the final selection of source-lens pairs, it is necessary to have a reasonable estimate of the lens mass in each case. In the left-hand panel of Figure 1, we plot absolute  $G$ -band magnitude  $M_G$  against  $G_{\text{BP}} - G_{\text{RP}}$  colour (using `PHOT_BP_MEAN_MAG` and `PHOT_RP_MEAN_MAG`) for the 38,717 lens stars in the final sample of source-lens pairs from Section 2.1. The absolute  $G$  magnitude is computed using:

$$M_G = G + 5 \log(\varpi_L) + 5 \quad (4)$$

where  $G$  is the apparent  $G$ -band mean magnitude (`PHOT_G_MEAN_MAG`). No attempt has been made to account for reddening and extinction in this plot.

<sup>3</sup><https://ssd.jpl.nasa.gov/horizons.cgi>

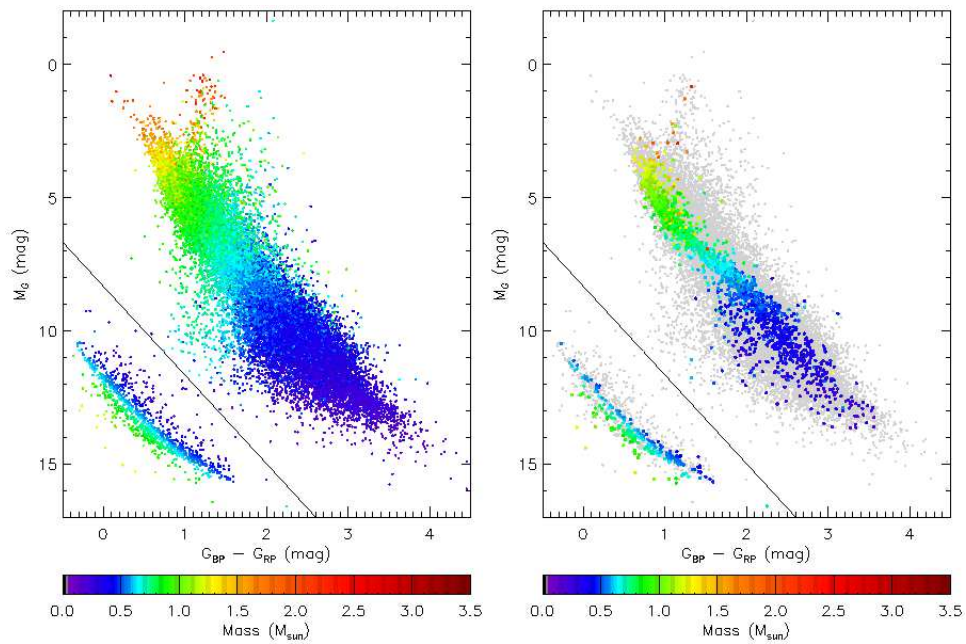


Figure 1: *Left:* Hertzsprung-Russell diagram of  $M_G$  versus  $G_{BP} - G_{RP}$  for the 38,717 lens stars in the final sample of source-lens pairs from Section 2.1. The continuous black line joining  $(-1,5)$  and  $(5,25)$  mag separates white dwarf stars from main sequence dwarfs/subdwarfs/giants (Kilic et al. 2018). The lens masses are indicated by the colour of the plot points (see the scale at the bottom of the panel). *Right:* Same as the left-hand panel for the 2,130 lens stars in the 2,509 microlensing events found in Section 2.3. The points from the left-hand panel are plotted in the background in light grey.



There are 1,007 white dwarf stars that lie below the continuous black line joining  $(-1,5)$  and  $(5,25)$  mag in Figure 1 (defined by Kilic et al. 2018). To estimate their masses, we interpolate the evolutionary cooling sequences for DA- and DB-type white dwarfs computed specifically for the *Gaia* passbands (Pierre Bergeron - private communication; Holberg & Bergeron 2006; Kowalski & Saumon 2006; Tremblay, Bergeron & Gianninas 2011; Bergeron et al. 2011). The mass estimates from the DA and DB cooling sequences are always very similar (to within  $\sim 1$ -15%) and for the purposes of predicting microlensing events, these differences are unimportant. Therefore, for each white dwarf lens star, we adopt the greater of the two mass estimates. The lens masses estimated by this method are indicated by the colours of the plot points in Figure 1.

There are 37,710 main sequence and giant stars that lie above the continuous line in Figure 1. We use the `isochrones` Python package (Morton 2015) to estimate the lens masses, which employs the MESA (Paxton et al. 2011, 2013, 2015) Isochrones and Stellar Track Library (MIST; Dotter 2016; Choi et al. 2016). For each lens star, we compute Sloan  $g$  and  $i$  magnitudes from  $G$ ,  $G_{BP}$  and  $G_{RP}$  via the relevant transformations given in Evans et al. (2018), and we provide  $\varpi_L$ ,  $G$ ,  $g$  and  $i$ , along with their uncertainties, as input to `isochrones`. Whenever possible, we bound-above the extinction prior in `isochrones` by using the `dustmaps` Python package with the Bayestar17 three-dimensional dust maps (Green et al. 2015, 2018). The `isochrones` package maximises the posterior probability of the fundamental parameters (mass, age, metallicity, distance, and extinction) for each lens star given the input data, and it samples the posterior distributions using the MCMC ensemble sampler `emcee` (Foreman-Mackey et al. 2013). We use 300 walkers which each execute a burn-in of 300 steps, iterate for a further 500 steps, and the last 100 of these steps are recorded. We adopt the median of the posterior sample as the estimate of the lens mass in each case. Again, the lens masses estimated by this method are indicated by the colours of the plot points in Figure 1.

### 2.3. Finding Microlensing Events

For each of the 42,572 source-lens pairs from Section 2.1, we perform 1,000 Monte Carlo simulations of the source and lens paths on the sky. Each simulation is generated using the following procedure:

1. We draw a set of astrometric parameters for the lens star from a multi-variate Gaussian distribution defined by the lens astrometric solution parameter values and their covariance matrix provided in GDR2. We do the same for the source star.
2. We use the lens mass estimate  $M_L$  from Section 2.2, and the lens and source parallaxes  $\varpi_L$  and  $\varpi_S$ , respectively, drawn in step (1), to calculate the Einstein radius  $\theta_E$  (Equation 1).
3. We compute the path of the source relative to the lens for the years 2020 to

2106, which fully encompasses the time period studied in this paper (25th July 2026 to 1st January 2100).

4. We compute the lens-to-source flux ratio  $f_L/f_S$  using the *Gaia* *G*-band photometry and we adopt *Gaia*'s resolution of 103 mas (Fabricius et al. 2016). We use these values along with the relative path computed in step (3) to calculate the amplitudes of the photometric and astrometric lensing signals in the unresolved (if necessary) and partially-resolved microlensing regimes (see Section 3 in this paper and Section 3 in B18).

We then calculate the median amplitude of each of the microlensing signals over all of the simulations for the source-lens pair. Collecting these results for the 42,572 source-lens pairs, we reject all source-lens pairs for which none of the median microlensing signal amplitudes exceed 0.4 mmag for photometric signals or 0.131 mas for astrometric signals (Section 2.1). We also reject all source-lens pairs for which the epoch  $t_0$  of the microlensing event peak falls outside of the time period 25th July 2026 to 1st January 2100. The characteristics of some of the predicted events are rather uncertain. To filter out these poorer-quality events, we reject all source-lens pairs for which the  $\pm 1$ -sigma range on  $t_0$  exceeds 0.8 years.

The final set of predicted microlensing events consists of 2,509 events caused by 2,130 unique lens stars. Eleven predicted events from B18 are present in this sample because they peak after 25th July 2026. These events are ME8, ME9, ME14, ME33, ME41, ME43, ME49, ME61, ME62, ME67, ME73, and their predicted properties presented in this almanac supersede those reported in B18 (e.g. ME62 has a  $\sim 15.9\%$  probability of yielding a photometric signal of at least  $\sim 0.03$  mag). We name the remaining events ME104-ME2601, following on from the last predicted event reported in Nielsen & Bramich (2018). The lenses consist of 213 white dwarfs and 1,917 main sequence and giant stars. In the right-hand panel of Figure 1, we plot the Hertzsprung-Russell diagram for the lenses in these microlensing events, with the lenses from the left-hand panel plotted in the background in light grey.

### 3. The Almanac

The almanac of predicted microlensing events for the 21st century<sup>4</sup> is provided as a table in electronic form with 99 columns and a single row per event. The table format and column meanings are defined in Tables 2 and 3, which also include an example row for event ME2395.

The following definitions relevant to the almanac are reported here for convenience, and the reader is referred to Section 3 of B18 for full details. For unresolved microlensing, the observed overall magnification  $A$  of the source and lens blend is

---

<sup>4</sup>Available at the Centre de Données astronomiques de Strasbourg: <http://cdsweb.u-strasbg.fr/>

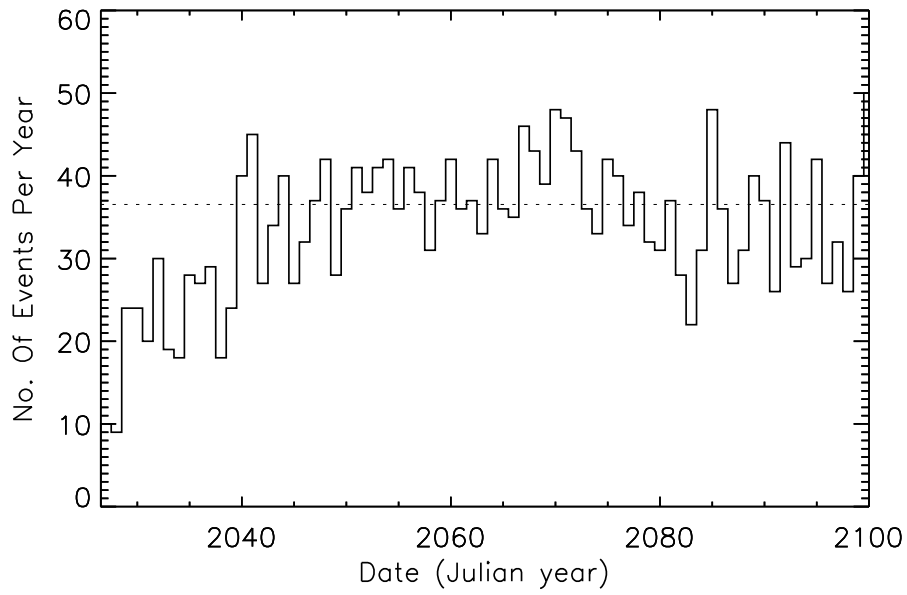


Figure 2: Number of predicted microlensing events per year as a function of Julian year in the almanac. The bin size is 1 year. The horizontal dotted line shows the mean event rate of  $\sim 36.5$  events per year from 2040 to 2100.

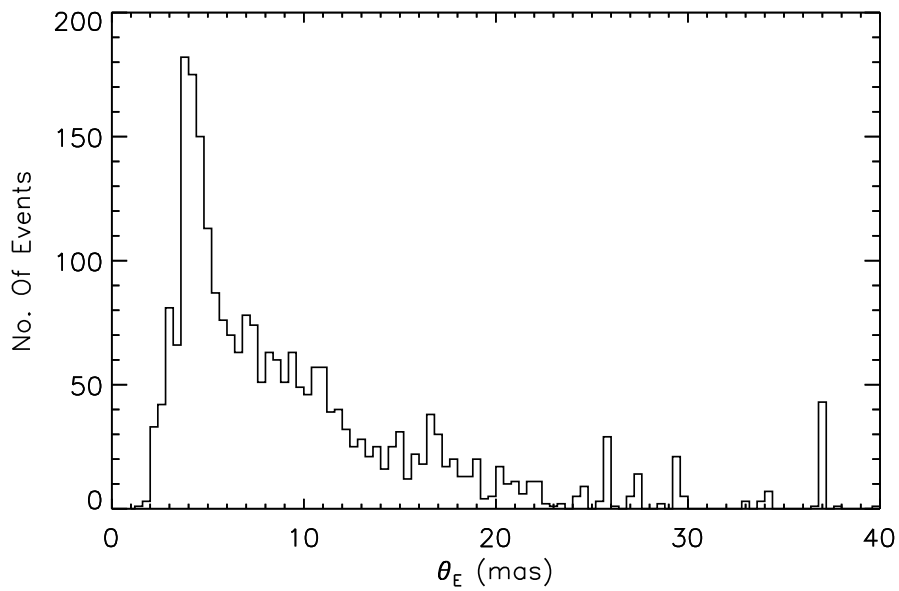


Figure 3: Histogram of  $\theta_E$  for the microlensing events in the almanac. The bin size is 0.4 mas.

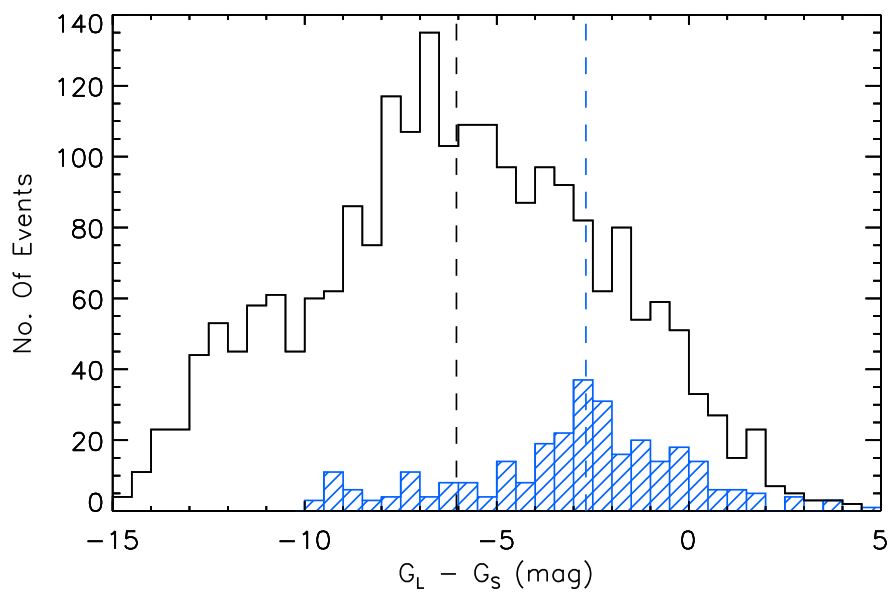


Figure 4: Histograms of the magnitude difference  $G_L - G_S$  for the microlensing events in the almanac for main sequence dwarfs/subdwarfs/giants (black histogram) and white dwarfs (blue histogram with striped bars). The bin size is 0.5 mag. The median values for each histogram are plotted as vertical dashed lines ( $-6.05$  and  $-2.68$  mag for the black and blue histograms, respectively).

given by:

$$A = \frac{u^2 + 2 + (f_L/f_S)u\sqrt{u^2 + 4}}{(1 + f_L/f_S)u\sqrt{u^2 + 4}} \quad (5)$$

For angular position vectors  $\vec{\phi}_S$  and  $\vec{\phi}_L$  on the celestial sphere corresponding to the source and the lens, respectively, one may calculate the normalised source-lens separation  $u$  via:

$$u = \left| \frac{\vec{\phi}_S - \vec{\phi}_L}{\theta_E} \right| \quad (6)$$

The normalised source-lens separation reaches a minimum of  $u = u_0$  at time  $t = t_0$ . The centroid shift due to microlensing in the unresolved regime is given by:

$$\delta_{\text{mic}} = \frac{\theta_E u}{1 + f_L/f_S} \left[ \frac{1 + (f_L/f_S) \left( u^2 + 3 - u\sqrt{u^2 + 4} \right)}{u^2 + 2 + (f_L/f_S)u\sqrt{u^2 + 4}} \right] \quad (7)$$

In the partially-resolved microlensing regime, the major source image is resolved from the blend of the minor source image and the lens. In this case, the major source image is magnified by  $A_1$  relative to the source flux and it is shifted from the nominal source position by an angular distance of  $\theta_2$ . Also, the blend of the minor source image and the lens is magnified by  $A_{\text{LL}_2}$  relative to the lens flux and the centroid is shifted from the nominal lens position by an angular distance of  $\theta_{\text{LL}_2}$ . These quantities are given by:

$$A_1 = \frac{u^2 + 2}{2u\sqrt{u^2 + 4}} + \frac{1}{2} \quad (8)$$

$$\theta_2 = \frac{\theta_E}{2} \left( \sqrt{u^2 + 4} - u \right) \quad (9)$$

$$A_{\text{LL}_2} = \frac{u^2 + 2 + (2(f_L/f_S) - 1)u\sqrt{u^2 + 4}}{2(f_L/f_S)u\sqrt{u^2 + 4}} \quad (10)$$

$$\theta_{\text{LL}_2} = \theta_E \left[ \frac{(u^2 + 1) \left( \sqrt{u^2 + 4} - u \right) - 2u}{u^2 + 2 + (2(f_L/f_S) - 1)u\sqrt{u^2 + 4}} \right] \quad (11)$$

It is important to note that in creating the almanac, no attempt has been made to identify binary stars (visual or unresolved) that may contaminate the lens and/or source stars in some of the predicted events. The effect of binarity on the predictions for affected source-lens pairs can range from negligible (e.g. if the orbital period is of the order of thousands of years) to invalidating a predicted event entirely (e.g. if the orbital period is of the order of a century). However, lens and source stars in this study were selected to have astrometric solutions that do not exhibit significant excess noise specifically to exclude the shorter period binary

stars from the sample. Hence, there should be relatively little contamination from binaries with periods of up to  $\sim 10 \times$  the GDR2 time baseline (i.e.  $\sim 20$  years).

In Figure 2, we plot the number of predicted microlensing events per year as a function of Julian year. The event rate increases until the year  $\sim 2040$ , whereafter it stabilises at  $\sim 36.5$  events/year (dotted line). We note that source-lens pairs in GDR2 must start out as resolved objects during the period over which the GDR2 data were acquired (25th July 2014 to 23rd May 2016), and that for GDR2, resolved source-lens pairs are separated by at least  $\sim 0.5''$  at the *Gaia* reference epoch (J2015.5; Arenou et al. 2018). Therefore, it takes a number of years before the majority of source-lens pairs can approach each other close enough to start producing microlensing events, resulting in the observed ramping-up of the event rate from 2015 to  $\sim 2040$ .

In Figure 3, we plot a histogram of the Einstein radius for the microlensing events in the almanac. The largest value of  $\theta_E$  is  $\sim 39.76$  mas for the event ME675 caused by the white dwarf lens star Wolf 28 (distance  $\sim 4.31$  pc). However, the majority of  $\theta_E$  values are below  $\sim 20$  mas, with a peak at  $\sim 4$  mas. The cut-off below  $\theta_E \approx 4$  mas is due to the fact that the more-distant slower-moving lenses do not have enough time before the year 2100 to fully approach potential source stars. In fact, all of the lenses in the almanac are closer than 1.9 kpc, and 95.9% of the lenses are closer than 500 pc.

In Figure 4, we plot two histograms of the magnitude difference  $G_L - G_S$  for the microlensing events in the almanac, where  $G_L$  and  $G_S$  are the mean  $G$ -band magnitudes for the lens and source stars, respectively. The black and blue histograms correspond to main sequence dwarfs/subdwarfs/giants and white dwarfs, respectively. Predicted events that are most favourable for follow-up observations are those where the lens is fainter than the source. There are 118 such events where the lens is a main sequence dwarf/subdwarf/giant star and 39 such events where the lens is a white dwarf star. The histograms, along with their median values, demonstrate that the contrast between a white dwarf lens and the source is typically considerably less than the contrast between a main sequence dwarf/subdwarf/giant lens and the source, indicating that predicted events with white dwarf lenses will generally be less challenging to observe.

With future *Gaia* data releases (e.g. GDR3 scheduled for late 2020), we intend to refine the predictions in the almanac and to add new predictions for stars that were not included in GDR2 (e.g. for the  $\sim 17\%$  of stars with proper motions greater than  $\sim 0.6$  arcsec  $\text{yr}^{-1}$  that are missing from GDR2 - Brown et al. 2018).

#### 4. A Few Highlights

The almanac contains 161 lenses that will cause at least two microlensing events each, and six lenses that will cause at least 10 events each (LAWD 37,

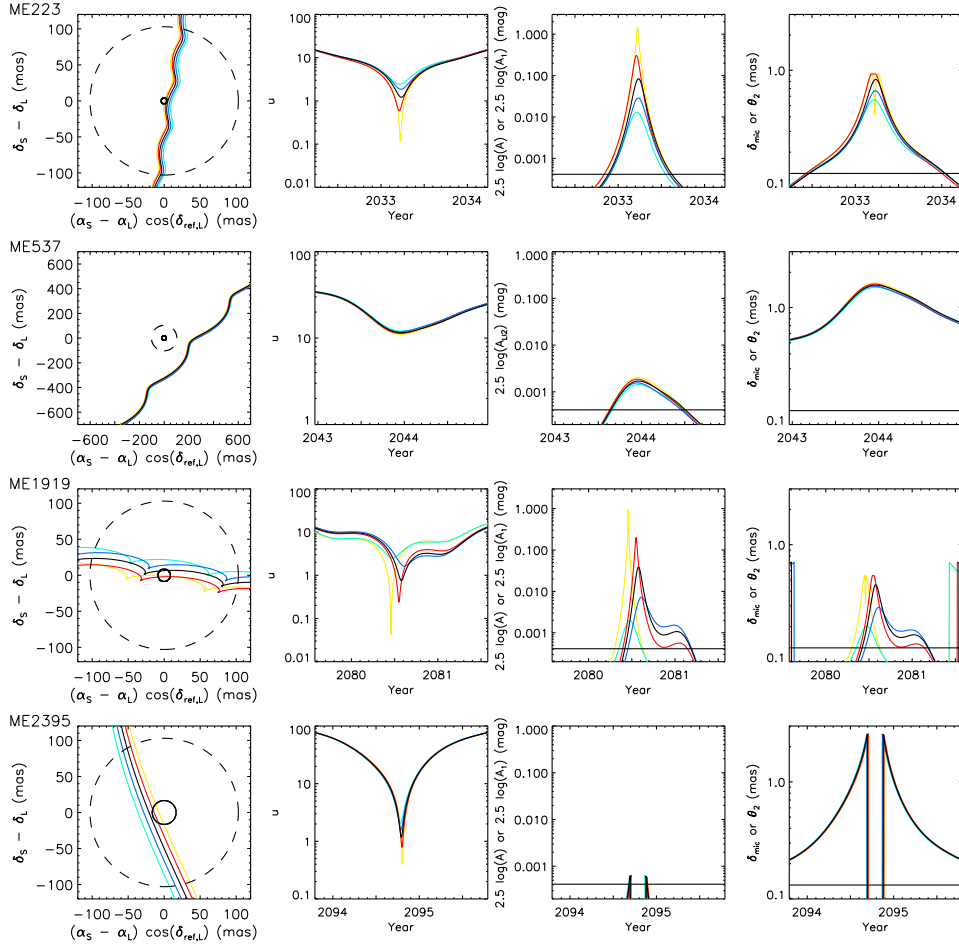


Figure 5: Microlensing events ME223, ME537, ME1919 and ME2395. In all panels, five curves are plotted with the colours yellow, red, black, blue, and cyan. Each curve corresponds to the 2.3, 15.9, 50, 84.1, and 97.7 percentiles, respectively, of the results of the Monte Carlo simulations performed in Section 2.3 after they have been ordered by increasing  $u_0$ . The yellow and cyan curves are plotted first, followed by the red and blue curves, and finally the black curve, which is why the black curve is the most visible when the individual curves are hard to distinguish. *Left-hand panels*: Path of the source star relative to the lens star. The Einstein ring is shown as a circle of radius  $\theta_E$  centred on the lens position (also plotted five times with five different colours). The resolution of *Gaia* is indicated as a circle of radius 103 mas centred on the lens position (dashed curve). *Middle left-hand panels*: Time-evolution of the normalised source-lens separation  $u$  ( $\theta_E$ ). *Middle right-hand panels*: Time-evolution of the photometric signals  $2.5 \log(A)$  (mag; unresolved regime) and  $2.5 \log(A_1)$  (mag; partially-resolved regime). Note that for ME537,  $2.5 \log(A_{LL_2})$  (mag; partially-resolved regime) is plotted instead. Definitions of  $A$ ,  $A_1$  and  $A_{LL_2}$  can be found in Section 3. The horizontal black line indicates the photometric precision limit of 0.4 mmag from Section 2.1. *Right-hand panels*: Time-evolution of the astrometric signals  $\delta_{\text{mic}}$  (mas; unresolved regime) and  $\theta_2$  (mas; partially-resolved regime). Definitions of  $\delta_{\text{mic}}$  and  $\theta_2$  can be found in Section 3. The horizontal black line indicates the astrometric precision limit of 0.131 mas from Section 2.1.

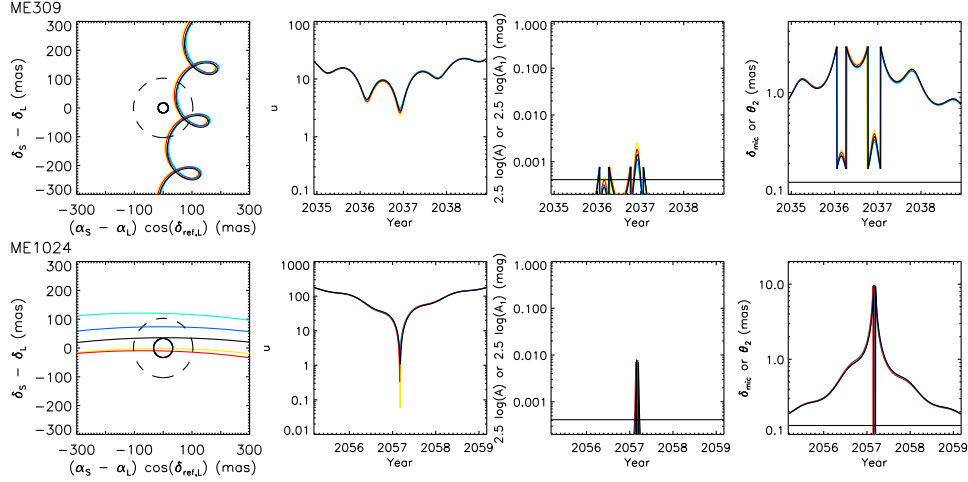


Figure 6: Microlensing events ME309 and ME1024. The format of the figure is the same as in Figure 5.

HD 180617<sup>5</sup>, GJ 674, HD 39194, HD 145417 and GJ 588). The lens that is most prolific at causing microlensing events is LAWD 37, which will produce 41 events between the years 2026 and 2100. Interestingly, of the six lenses mentioned, GJ 674 and HD 39194 have one and three confirmed planetary companions, respectively (Bonfils et al. 2007; Mayor et al. 2011). Projected on the sky, these planets lie at separations of the order of  $\sim 1$ -10 mas from their host stars. Unfortunately, GJ 674 will not approach any source stars close enough to produce a photometric event (even though it will cause four excellent astrometric microlensing events with source deflections greater than  $\sim 3$  mas). However, HD 39194 will approach a source star close enough to probe its planetary system in the event ME2395.

HD 39194 is a spectroscopically confirmed K0 dwarf star (Gray et al. 2006) with  $G_L \approx 7.85$  mag that lies in the direction of the Large Magellanic Cloud. The source star in event ME2395 is nearly 12 magnitudes fainter with  $G_S \approx 19.8$  mag. The event will peak on 16th October 2094 ( $\pm 3$  d). It will achieve a maximum source deflection of  $\sim 2.6$  mas and it will also exhibit a small photometric signal ( $\sim 0.7$  mmag). Both signals will be highly suppressed in the unresolved microlensing regime. Figure 5 illustrates how the event will unfold. The jumps in the photometric and astrometric curves are due to the event switching between partially-resolved and unresolved microlensing at the *Gaia* resolution of 103 mas. Clearly this behaviour is telescope/instrument dependent. The probability that the source and the lens will approach each other to within an angular distance of less than  $2\theta_E \approx 33.1$  mas is 97.2%. This event clearly demonstrates the power of *Gaia*

<sup>5</sup>This star is the primary in a visual binary (separation  $74''$ ; van Biesbroeck 1961) where the star vB 10 is the secondary component. vB 10 will also cause microlensing events in the coming years and the relevant predictions are presented in Nielsen & Bramich (2018).



astrometry for making reliable microlensing event predictions far into the future ( $\sim 76$  years in this case), and well after the authors will have passed away.

ME223 (Figure 5) is extremely likely to exhibit an easily detectable photometric signal ( $\pm 2$ -sigma range for  $\Delta A$  is  $\sim 0.013$ - $1.657$  mag) while also yielding a strong astrometric signal ( $\sim 0.84$  mas). It also has the potential to become a high-magnification microlensing event sensitive to planetary companions to the lens ( $P(u_0 < 1) = 0.363$ ). The lens star (not in SIMBAD<sup>6</sup>) is a main sequence star (likely K dwarf;  $\sim 0.6 M_\odot$ ) at  $\sim 253$  pc with  $G_L \approx 14.62$  mag that is only  $\sim 0.62$  mag brighter than the source star (at  $\sim 2.4$  kpc; unfortunately the source has no colour information in GDR2). The event will peak on 28th March 2033 ( $\pm 8$  d).

ME537 will be a very rare event in that the blend of the lens and the minor source image will brighten by  $\sim 1.7 \pm 0.2$  mmag due to the appearance of the minor source image as the event unfolds purely in the partially-resolved microlensing regime (Figure 5). In contrast, the brightening of the source will be much smaller at  $\sim 0.1$  mmag. This will occur because the source star is  $\sim 3.66$  mag brighter than the lens in the  $G$ -band ( $G_L \approx 17.44$  mag and  $G_S \approx 13.78$  mag), the Einstein radius is reasonably large ( $\theta_E \approx 18.1$  mas), and the lens will pass close to the source ( $\theta_E u_0 \approx 209$  mas) but the event will still remain in the partially-resolved regime (at least for some space telescopes like *Gaia* and *HST*). The event will be even more favourable in redder wavebands because the lens star (white dwarf; PM J07228-3042) is bluer than the source star (not in SIMBAD). Apart from the photometric signal for the lens, the event will exhibit a source deflection of  $\sim 1.54$  mas. The event peak will occur on 17th Dec 2043 ( $\pm 3$  d). There are only two other events similar to ME537, although they are not as favourable. These events are ME1609 and ME2252.

ME1919 is an interesting event because the photometric and astrometric signals will be double-peaked (Figure 5) due to the interplay between the lens parallax motion and its proper motion, and also because the lens will pass very close to the source star ( $P(u_0 < 1) = 0.616$ ). The event has the potential to achieve high-magnification, although the fact that the lens is  $\sim 2.95$  mag brighter than the source will suppress the signal (redder wavebands are more favourable). The first peak will occur on 17th July 2080 ( $\pm 26$  d). The lens (not in SIMBAD) is a main sequence star (likely late-K/early-M dwarf;  $\sim 0.5 M_\odot$ ).

Perhaps the funkiest event in the almanac is ME309 which will be caused by the DA6.6 white dwarf WD 1223-659 (Gianninas, Bergeron & Ruiz 2011). The relative source-lens motion proceeds in loops due to the large lens parallax motion and its relatively slow proper motion. This will result in multiple peaks in both the photometric and astrometric signals over time (amplitudes  $\sim 1$  mmag and  $\sim 2.8$  mas, respectively; Figure 6). The event will reach its highest two peaks during the year 2036. Unfortunately, WD 1223-659 is brighter than the source star by  $\sim 2.96$  mag in the  $G$ -band which will suppress the microlensing signals when the event enters

---

<sup>6</sup><http://simbad.u-strasbg.fr/simbad/>

the unresolved regime. In this regard, it will be better to observe the event in redder wavebands.

Finally, ME1024 is the event in the almanac that will exhibit the largest amplitude astrometric signal ( $\sim 9.70 \pm 0.04$  mas) because it has a large Einstein radius ( $\theta_E \approx 33.1$  mas) and the source is very likely to pass within an angular distance of  $2\theta_E$  from the lens ( $P(u_0 < 2) = 0.801$ ). There may also be an associated photometric signal of  $\sim 8$  mmag (Figure 6). The lens star GJ 15 A is a spectroscopically confirmed M1.0 dwarf star (Trifonov et al. 2018) at a distance of  $\sim 3.56$  pc that has a  $\sim 5$  Earth-mass planet in an  $\sim 11.4$  d orbit (Howard et al. 2014). It is part of a visual binary with an M3.5 companion (GJ 15 B; Lépine et al. 2013) that has an orbital period of  $\sim 1250$  years (Romanenko & Kiselev 2014). Since the peak of the event will occur in  $\sim 39$  years time on 7th March 2057 ( $\pm 7$  d), the binary motion may somewhat affect the details of the event prediction presented here. While the photometric event may or may not occur as a consequence, the amplitude of the astrometric signal is unlikely to change much since it is much less dependent on a precise source-lens alignment. In the unresolved microlensing regime, the lens star will highly suppress the microlensing signals since it is  $\sim 13.5$  mag brighter than the source ( $G_L \approx 7.22$  mag and  $G_S \approx 20.75$  mag). The almanac contains various similar very high amplitude astrometric microlensing events.

The predicted events highlighted in this section illustrate how the current and future versions of the almanac have the potential to provide an invaluable resource for microlensing studies.

**Acknowledgements.** We thank the anonymous referee for taking the time to review this paper and for providing insightful comments that served to improve the content. DMB acknowledges the support of the NYU Abu Dhabi Research Enhancement Fund under grant RE124. MBN is supported by NYUAD Institute grant G1502. Many of the calculations performed in this paper employed code from the DanIDL library of IDL routines (Bramich 2017) available at <http://www.danidl.co.uk>. We are grateful to Pierre Bergeron for providing the white dwarf cooling models in the *Gaia* passbands. This research was carried out on the High Performance Computing resources at New York University Abu Dhabi. Thanks goes to Nasser Al Ansari, Muataz Al Barwani, Guowei He and Fayizal Mohammed Kunhi for their excellent support. We would also like to thank the Solar System Dynamics Group at the Jet Propulsion Laboratory for providing the Horizons On-Line Ephemeris System. We made extensive use of the SIMBAD and VizieR web-resources as provided by the Centre de Données astronomiques de Strasbourg. This work has made use of data from the European Space Agency (ESA) mission *Gaia* (<https://www.cosmos.esa.int/gaia>), processed by the *Gaia* Data Processing and Analysis Consortium (DPAC, <https://www.cosmos.esa.int/web/gaia/dpac/consortium>). Funding for the DPAC has been provided by national institutions, in particular the institutions participating in

the *Gaia* Multilateral Agreement.

## REFERENCES

- Arenou F. et al. 2018, *A&A*, **616**, A17.  
 Beaulieu J.-P. et al. 2006, *Nature*, **439**, 437.  
 Bergeron P. et al. 2011, *ApJ*, **737**, 28.  
 Bonfils X. et al. 2007, *A&A*, **474**, 293.  
 Bramich D.M. 2018, *A&A*, **Accepted**, (B18).  
 Bramich D.M. 2017, *Astrophysics Source Code Library*, **record ascl:1709.005**, .  
 Brown A.G.A. et al. 2018, *A&A*, **in press**, .  
 Choi J., Dotter A., Conroy C., Cantiello M., Paxton B. & Johnson B.D. 2016, *ApJ*, **823**, 102.  
 Dotter A. 2016, *ApJS*, **222**, 8.  
 Evans D.W. et al. 2018, *A&A*, **616**, A4.  
 Explanatory Supplement to the Astronomical Almanac 2013, *3rd edition*, ed. S. Urban & P.K. Seidelmann (University Science Books, Mill Valley, California), **p263**, .  
 Fabricius C. et al. 2016, *A&A*, **595**, A3.  
 Feibelman W.A. 1966, *Science*, **151**, 73.  
 Foreman-Mackey D., Hogg D.W., Lang D. & Goodman J. 2013, *PASP*, **125**, 306.  
 Gianninas A., Bergeron P. & Ruiz M.T. 2011, *ApJ*, **743**, 138.  
 Gray R.O., Corbally C.J., Garrison R.F., McFadden M.T., Bubar E.J., McGahee C.E., O'Donoghue A.A. & Knox E.R. 2006, *AJ*, **132**, 161.  
 Green G.M. et al. 2015, *ApJ*, **810**, 25.  
 Green G.M. et al. 2018, *MNRAS*, **478**, 651.  
 Hoffmann S.L. & Anderson J. 2017, <http://www.stsci.edu/hst/acs/documents/isrs/isr1708.pdf>, .  
 Høg E., Novikov I.D. & Polnarev A.G. 1995, *A&A*, **294**, 287.  
 Holberg J.B. & Bergeron P. 2006, *AJ*, **132**, 1221.  
 Howard A.W. et al. 2014, *ApJ*, **794**, 51.  
 Kains N. et al. 2017, *ApJ*, **843**, 145.  
 Kilic M., Hambly N.C., Bergeron P., Genest-Beaulieu C. & Rowell N. 2018, *MNRAS*, **479**, 113.  
 Klüter J., Bastian U., Demleitner M. & Wambsgans J. 2018, *A&A*, **615**, 11.  
 Kowalski P.M. & Saumon D. 2006, *ApJ*, **651**, 137.  
 Lépine S., Hilton E.J., Mann A.W., Wilde M., Rojas-Ayala B., Cruz K.L. & Gaidos E. 2013, *AJ*, **145**, 102.  
 Lindegren L. et al. 2016, *A&A*, **595**, A4.  
 Lindegren L. et al. 2018, *A&A*, **616**, A2.  
 Mayor M. et al. 2011, *arXiv*, **1109.2497**, .  
 McGill P., Smith L.C., Evans N.W., Belokurov V. & Smart R.L. 2018, *MNRAS*, **478**, 29.  
 Miyamoto M. & Yoshii Y. 1995, *AJ*, **110**, 1427.  
 Morton T.D. 2015, *Astrophysics Source Code Library*, **ascl:1503.010**, .  
 Mustill A.J., Davies M.B. & Lindegren L. 2018, *A&A*, **submitted**, .  
 Nielsen M.B. & Bramich D.M. 2018, *AcA*, **submitted**, .  
 Ofek E.O. 2018, *ApJ*, **submitted**, .  
 Paxton B., Bildsten L., Dotter A., Herwig F., Lesaffre P. & Timmes F. 2011, *ApJS*, **192**, 3.  
 Paxton B. et al. 2013, *ApJS*, **208**, 4.  
 Paxton B. et al. 2015, *ApJS*, **220**, 15.  
 Proft S., Demleitner M. & Wambsgans J. 2011, *A&A*, **536**, 50.  
 Prusti T. et al. 2016, *A&A*, **595**, A1.  
 Romanenko L.G. & Kiselev A.A. 2014, *Astron. Rep.*, **58**, 30.  
 Rybicki K.A., Wyrzykowski Ł., Klencki J., de Bruijne J., Belczyński K. & Chruślińska M. 2018, *MNRAS*, **476**, 2013.

- Sahu K.C. et al. 2017, *Science*, **356**, 1046.  
Salim S. & Gould A. 2000, *ApJ*, **539**, 241.  
Torres G., Andersen J. & Giménez A. 2010, *Astron. Astrophys. Rev.*, **18**, 67.  
Tremblay P.-E., Bergeron P. & Gianninas A. 2011, *ApJ*, **730**, 128.  
Trifonov T. et al. 2018, *A&A*, **609**, 117.  
Udalski A. et al. 2005, *ApJ*, **628**, 109.  
van Biesbroeck G. 1961, *AJ*, **66**, 528.  
Walker M.A. 1995, *ApJ*, **453**, 37.  
White R.L. 2006, <http://www.stsci.edu/hst/acs/documents/isrs/isr0605.pdf>, . .  
Yee J.C. et al. 2009, *ApJ*, **703**, 2082.  
Yoo J. et al. 2004, *ApJ*, **603**, 139.  
Zhu W. et al. 2016, *ApJ*, **825**, 60.

Table 2: Almanac of predicted microlensing events with peaks occurring between 25th July 2026 ( $t = 2461246.5$  BJD[TDB]) and 1st January 2100 ( $t = 2488069.5$  BJD[TDB]). Events are ordered by increasing median epoch of the peak  $t_0$  (column 63). The values in columns 38-99 are computed from the 1,000 Monte Carlo simulations performed for each source-lens pair in Section 2.3.

Column Number	Column Name	Example Event ME2395	Description
1	Event Name	ME2395	The name of the predicted microlensing event
2	Lens Spectral Type	MS	Lens star type: WD = white dwarf, MS = main sequence/subdwarf/giant
3	Lens GDR2 ID	4657193606465368704	Lens GDR2 source ID
4	$\alpha_{\text{ref,L}}$	86.1290710186	Lens right ascension at the reference epoch J2015.5 (deg)
5	$\sigma[\alpha_{*,\text{ref,L}}]$	0.042	Uncertainty on $\alpha_{\text{ref,L}} \cos(\delta_{\text{ref,L}})$ (mas)
6	$\delta_{\text{ref,L}}$	-70.1382377141	Lens declination at the reference epoch J2015.5 (deg)
7	$\sigma[\delta_{\text{ref,L}}]$	0.048	Uncertainty on $\delta_{\text{ref,L}}$ (mas)
8	$\mu_{\alpha*,\text{L}}$	-309.424	Lens proper motion in right ascension (mas/year)
9	$\sigma[\mu_{\alpha*,\text{L}}]$	0.078	Uncertainty on $\mu_{\alpha*,\text{L}}$ (mas/year)
10	$\mu_{\delta,\text{L}}$	1238.780	Lens proper motion in declination (mas/year)
11	$\sigma[\mu_{\delta,\text{L}}]$	0.098	Uncertainty on $\mu_{\delta,\text{L}}$ (mas/year)
12	$\varpi_{\text{L}}$	37.860	Lens parallax (mas)
13	$\sigma[\varpi_{\text{L}}]$	0.047	Uncertainty on $\varpi_{\text{L}}$ (mas)
14	$G_{\text{L}}$	7.8520	Lens $G$ -band mean magnitude (mag)
15	$\sigma[G_{\text{L}}]$	0.0002	Uncertainty on $G_{\text{L}}$ (mag)
16	$G_{\text{BP,L}}$	8.2816	Lens $G_{\text{BP}}$ -band mean magnitude (mag)
17	$\sigma[G_{\text{BP,L}}]$	0.0016	Uncertainty on $G_{\text{BP,L}}$ (mag)
18	$G_{\text{RP,L}}$	7.3085	Lens $G_{\text{RP}}$ -band mean magnitude (mag)
19	$\sigma[G_{\text{RP,L}}]$	0.0039	Uncertainty on $G_{\text{RP,L}}$ (mag)
20	$M_{\text{L}}$	0.89	Lens mass estimate ( $M_{\odot}$ )
21	Source GDR2 ID	4657195114116751360	Source GDR2 source ID
22	$\alpha_{\text{ref,S}}$	86.1090246836	Source right ascension at the reference epoch J2015.5 (deg)
23	$\sigma[\alpha_{*,\text{ref,S}}]$	0.904	Uncertainty on $\alpha_{\text{ref,S}} \cos(\delta_{\text{ref,S}})$ (mas)
24	$\delta_{\text{ref,S}}$	-70.1109601904	Source declination at the reference epoch J2015.5 (deg)
25	$\sigma[\delta_{\text{ref,S}}]$	1.194	Uncertainty on $\delta_{\text{ref,S}}$ (mas)
26	$\mu_{\alpha*,\text{S}}$	-	Source proper motion in right ascension (mas/year)
27	$\sigma[\mu_{\alpha*,\text{S}}]$	-	Uncertainty on $\mu_{\alpha*,\text{S}}$ (mas/year)
28	$\mu_{\delta,\text{S}}$	-	Source proper motion in declination (mas/year)
29	$\sigma[\mu_{\delta,\text{S}}]$	-	Uncertainty on $\mu_{\delta,\text{S}}$ (mas/year)
30	$\varpi_{\text{S}}$	-	Source parallax (mas)
31	$\sigma[\varpi_{\text{S}}]$	-	Uncertainty on $\varpi_{\text{S}}$ (mas)
32	$G_{\text{S}}$	19.7920	Source $G$ -band mean magnitude (mag)
33	$\sigma[G_{\text{S}}]$	0.0094	Uncertainty on $G_{\text{S}}$ (mag)
34	$G_{\text{BP,S}}$	-	Source $G_{\text{BP}}$ -band mean magnitude (mag)
35	$\sigma[G_{\text{BP,S}}]$	-	Uncertainty on $G_{\text{BP,S}}$ (mag)
36	$G_{\text{RP,S}}$	-	Source $G_{\text{RP}}$ -band mean magnitude (mag)
37	$\sigma[G_{\text{RP,S}}]$	-	Uncertainty on $G_{\text{RP,S}}$ (mag)
38	2.3%tile $\theta_{\text{E}}$	16.527	2.3 percentile of the Einstein radius (mas)
39	15.9%tile $\theta_{\text{E}}$	16.537	15.9 percentile of the Einstein radius (mas)
40	Median $\theta_{\text{E}}$	16.547	Median of the Einstein radius (mas)
41	84.1%tile $\theta_{\text{E}}$	16.557	84.1 percentile of the Einstein radius (mas)
42	97.7%tile $\theta_{\text{E}}$	16.567	97.7 percentile of the Einstein radius (mas)
43	2.3%tile $u_0$	0.40	2.3 percentile of the minimum normalised source-lens separation $u_0$ ( $\theta_{\text{E}}$ )
44	15.9%tile $u_0$	0.79	15.9 percentile of the minimum normalised source-lens separation $u_0$ ( $\theta_{\text{E}}$ )
45	Median $u_0$	1.18	Median of the minimum normalised source-lens separation $u_0$ ( $\theta_{\text{E}}$ )
46	84.1%tile $u_0$	1.59	84.1 percentile of the minimum normalised source-lens separation $u_0$ ( $\theta_{\text{E}}$ )
47	97.7%tile $u_0$	2.05	97.7 percentile of the minimum normalised source-lens separation $u_0$ ( $\theta_{\text{E}}$ )
48	$P(u_0 < 1)$	0.338	Probability that the event will have $u_0 < 1$
49	$P(u_0 < 2)$	0.972	Probability that the event will have $u_0 < 2$
50	$P(u_0 < 5)$	1.000	Probability that the event will have $u_0 < 5$
51	$P(u_0 < 10)$	1.000	Probability that the event will have $u_0 < 10$

Table 3: Table 2 continued. Definitions of  $A$ ,  $A_1$ ,  $A_{LI_2}$ ,  $\delta_{mic}$ ,  $\theta_2$  and  $\theta_{LI_2}$  can be found in Section 3.

Column Number	Column Name	Example Event ME2395	Description
52	2.3%tile $\theta_E u_0$	6.67	2.3 percentile of the minimum source-lens separation $\theta_E u_0$ (mas)
53	15.9%tile $\theta_E u_0$	13.00	15.9 percentile of the minimum source-lens separation $\theta_E u_0$ (mas)
54	Median $\theta_E u_0$	19.47	Median of the minimum source-lens separation $\theta_E u_0$ (mas)
55	84.1%tile $\theta_E u_0$	26.30	84.1 percentile of the minimum source-lens separation $\theta_E u_0$ (mas)
56	97.7%tile $\theta_E u_0$	33.83	97.7 percentile of the minimum source-lens separation $\theta_E u_0$ (mas)
57	$P(\theta_E u_0 < 100 \text{ mas})$	1.000	Probability that the event will have $\theta_E u_0 < 100 \text{ mas}$
58	$P(\theta_E u_0 < 200 \text{ mas})$	1.000	Probability that the event will have $\theta_E u_0 < 200 \text{ mas}$
59	$P(\theta_E u_0 < 500 \text{ mas})$	1.000	Probability that the event will have $\theta_E u_0 < 500 \text{ mas}$
60	$P(\theta_E u_0 < 1000 \text{ mas})$	1.000	Probability that the event will have $\theta_E u_0 < 1000 \text{ mas}$
61	2.3%tile $t_0$	2094.77563	2.3 percentile of the epoch of the event peak $t_0$ (Julian year)
62	15.9%tile $t_0$	2094.78296	15.9 percentile of the epoch of the event peak $t_0$ (Julian year)
63	Median $t_0$	2094.78912	Median of the epoch of the event peak $t_0$ (Julian year)
64	84.1%tile $t_0$	2094.79582	84.1 percentile of the epoch of the event peak $t_0$ (Julian year)
65	97.7%tile $t_0$	2094.80240	97.7 percentile of the epoch of the event peak $t_0$ (Julian year)
66	2.3%tile $\Delta(A, A_1)$	0.0007	2.3 percentile of the difference between the minimum and maximum source magnifications over the time period adopted in this paper (mag)
67	15.9%tile $\Delta(A, A_1)$	0.0007	15.9 percentile of $\Delta(A, A_1)$ (mag)
68	Median $\Delta(A, A_1)$	0.0007	Median of $\Delta(A, A_1)$ (mag)
69	84.1%tile $\Delta(A, A_1)$	0.0007	84.1 percentile of $\Delta(A, A_1)$ (mag)
70	97.7%tile $\Delta(A, A_1)$	0.0007	97.7 percentile of $\Delta(A, A_1)$ (mag)
71	2.3%tile $T[\Delta(A, A_1)]$	13.07	2.3 percentile of the amount of time that the source spends with its magnification above $\min\{A, A_1\} + \Delta(A, A_1)/2$ (d)
72	15.9%tile $T[\Delta(A, A_1)]$	13.20	15.9 percentile of $T[\Delta(A, A_1)]$ (d)
73	Median $T[\Delta(A, A_1)]$	13.37	Median of $T[\Delta(A, A_1)]$ (d)
74	84.1%tile $T[\Delta(A, A_1)]$	13.62	84.1 percentile of $T[\Delta(A, A_1)]$ (d)
75	97.7%tile $T[\Delta(A, A_1)]$	13.95	97.7 percentile of $T[\Delta(A, A_1)]$ (d)
76	$P(\Delta(A, A_1) > 0.4 \text{ mmag})$	1.000	Probability that the event will yield a source magnification above 0.4 mmag
77	2.3%tile $\Delta A_{LI_2}$	0.0000	2.3 percentile of the difference between the minimum and maximum lens magnifications over the time period adopted in this paper (mag)
78	15.9%tile $\Delta A_{LI_2}$	0.0000	15.9 percentile of $\Delta A_{LI_2}$ (mag)
79	Median $\Delta A_{LI_2}$	0.0000	Median of $\Delta A_{LI_2}$ (mag)
80	84.1%tile $\Delta A_{LI_2}$	0.0000	84.1 percentile of $\Delta A_{LI_2}$ (mag)
81	97.7%tile $\Delta A_{LI_2}$	0.0000	97.7 percentile of $\Delta A_{LI_2}$ (mag)
82	$P(\Delta A_{LI_2} > 0.4 \text{ mmag})$	0.000	Probability that the event will yield a lens magnification above 0.4 mmag
83	2.3%tile $\Delta(\delta_{mic}, \theta_2)$	2.586	2.3 percentile of the difference between the minimum and maximum source astrometric shifts over the time period adopted in this paper (mas)
84	15.9%tile $\Delta(\delta_{mic}, \theta_2)$	2.589	15.9 percentile of $\Delta(\delta_{mic}, \theta_2)$ (mas)
85	Median $\Delta(\delta_{mic}, \theta_2)$	2.592	Median of $\Delta(\delta_{mic}, \theta_2)$ (mas)
86	84.1%tile $\Delta(\delta_{mic}, \theta_2)$	2.595	84.1 percentile of $\Delta(\delta_{mic}, \theta_2)$ (mas)
87	97.7%tile $\Delta(\delta_{mic}, \theta_2)$	2.598	97.7 percentile of $\Delta(\delta_{mic}, \theta_2)$ (mas)
88	2.3%tile $T[\Delta(\delta_{mic}, \theta_2)]$	67.22	2.3 percentile of the amount of time that the source spends with its astrometric shift above $\min\{\delta_{mic}, \theta_2\} + \Delta(\delta_{mic}, \theta_2)/2$ (d)
89	15.9%tile $T[\Delta(\delta_{mic}, \theta_2)]$	67.62	15.9 percentile of $T[\Delta(\delta_{mic}, \theta_2)]$ (d)
90	Median $T[\Delta(\delta_{mic}, \theta_2)]$	68.20	Median of $T[\Delta(\delta_{mic}, \theta_2)]$ (d)
91	84.1%tile $T[\Delta(\delta_{mic}, \theta_2)]$	68.97	84.1 percentile of $T[\Delta(\delta_{mic}, \theta_2)]$ (d)
92	97.7%tile $T[\Delta(\delta_{mic}, \theta_2)]$	70.05	97.7 percentile of $T[\Delta(\delta_{mic}, \theta_2)]$ (d)
93	$P(\Delta(\delta_{mic}, \theta_2) > 0.131 \text{ mas})$	1.000	Probability that the event will yield a source astrometric shift above 0.131 mas
94	2.3%tile $\Delta\theta_{LI_2}$	0.000	2.3 percentile of the difference between the minimum and maximum lens astrometric shifts over the time period adopted in this paper (mas)
95	15.9%tile $\Delta\theta_{LI_2}$	0.000	15.9 percentile of $\Delta\theta_{LI_2}$ (mas)
96	Median $\Delta\theta_{LI_2}$	0.000	Median of $\Delta\theta_{LI_2}$ (mas)
97	84.1%tile $\Delta\theta_{LI_2}$	0.000	84.1 percentile of $\Delta\theta_{LI_2}$ (mas)
98	97.7%tile $\Delta\theta_{LI_2}$	0.000	97.7 percentile of $\Delta\theta_{LI_2}$ (mas)
99	$P(\Delta\theta_{LI_2} > 0.131 \text{ mas})$	0.000	Probability that the event will yield a lens astrometric shift above 0.131 mas